Journal of Environmental Chemical Engineering 11 (2023) 109898

Contents lists available at ScienceDirect

Journal of Environmental Chemical Engineering

journal homepage: www.elsevier.com/locate/jece

PVDF membranes containing alkyl and perfluoroalkyl-functionalized graphene nanosheets for improved membrane distillation

Jose Miguel Luque-Alled [a,c,d], Sebastian Leaper [a], Ahmed Abdel-Karim [a,b], Clara Skuse [a], Patricia Gorgojo [a,c,d,*]

[a] Department of Chemical Engineering, Faculty of Science and Engineering, The University of Manchester, Manchester M13 9PL, United Kingdom
[b] Water Pollution Research Department, National Research Centre, 33 El Buhouth St., Dokki, 12622 Giza, Egypt
[c] Instituto de Nanociencia y Materiales de Aragón (INMA) CSIC-Universidad de Zaragoza, Zaragoza 50018, Spain
[d] Departamento de Ingeniería Química y Tecnologías del Medio Ambiente, Universidad de Zaragoza, Zaragoza 50009, Spain

ARTICLE INFO

Editor: Yunho Lee

Keywords:
Membrane distillation
Hydrophobic functionalization
Graphene oxide
Polyvinylidene fluoride
Desalination

ABSTRACT

Polyvinylidene fluoride (PVDF) membranes containing hydrophobic graphene nanofillers were prepared and tested for membrane distillation applications. The nanofillers were obtained by a two-step process: 1st) chemical grafting of hydrophobic molecules, either octylamine (OA) or perfluorooctylamine (PFOA), to graphene oxide (GO) nanosheets, and 2nd) chemical reduction of functionalized GO (rGO) to remove unreacted oxygen-containing functional groups. This resulted in OA-functionalized reduced GO (OA-rGO) and PFOA-functionalized rGO (PFOA-rGO). The addition of these nanomaterials to PVDF membranes prepared by the phase inversion process led to an increase in the membrane contact angle, and therefore higher hydrophobicity, as well as an increase in the membrane porosity. When comparing both nanofillers, OA-rGO and PFOA-rGO, the latter was more efficient in achieving higher contact angles due to the presence of fluorine atoms, whereas OA-rGO led to a greater enhancement in membrane porosity as compared to PFOA-rGO. MMMs containing 0.7 wt% nanofiller loadings of OA-rGO and PFOA-rGO achieved the highest water fluxes of 9.1 and 8.8 L m^{-2} h^{-1}, respectively and salt rejection above 99.9%, which was monitored for at least 162 h of operation for the former. In comparison with pure PVDF (flux of 5 L m^{-2} h^{-1}), the addition of OA-rGO and PFOA-rGO nanofillers results in a flux increment of 82% and 76%, respectively.

1. Introduction

The world is currently facing water scarcity due to population growth and extreme weather events. Currently only 1% of global water supplies can be used for human consumption [1], with the remainder either being highly saline (i.e. seawater or brackish water) or locked up in ice formations such as mountain snow caps or polar ice sheets. Since 97.5% of the total water in the planet is saline water, desalination of seawater and brackish water shows enormous potential [1]. Although the desalination process is energetically expensive [2], numerous desalination plants are already under operation producing high quality water, mainly in coastal areas or when surface and ground water is not available [2]. To cover basic needs for future generations, more sustainable and energy-efficient technologies capable of producing larger fresh water streams are required.

Membrane distillation (MD) consists of a thermally based process mostly used for desalination purposes in which water vapor travels through a hydrophobic membrane that prevents liquid water, having salts, metals or organic contaminants dissolved, from penetrating the membrane. MD presents several advantages over reverse osmosis (RO) processes, the state-of-the-art desalination technology, including lower required transmembrane pressures involved, less demanding membrane characteristics (e.g. lower mechanical properties and wide pore sizes), lower fouling propensity and less pretreatment processes, possibility of using waste heat reducing energy consumption, and capability of treating a wide range of wastewaters streams [3,4]. As compared to other desalination technologies which do not involve the use of membranes (e.g. multistage flash distillation, multi-effect distillation and mechanical vapor compression), MD offers several advantages such as: i) capable of treating high feed salinities [5], ii) low footprint due to high compactness and small-scale units [6], iii) operating temperature below water boiling point, and iv) allows for the use of renewable energy

* Corresponding author at: Departamento de Ingeniería Química y Tecnologías del Medio Ambiente, Universidad de Zaragoza, Zaragoza 50009, Spain.
E-mail address: p.gorgojo@unizar.es (P. Gorgojo).

https://doi.org/10.1016/j.jece.2023.109898
Received 20 September 2022; Received in revised form 2 April 2023; Accepted 11 April 2023
Available online 12 April 2023

sources [5,7,8]. However, the main limitations of MD are related to low membrane flux (i.e. low water outputs), membrane wetting and high thermal energy consumption [9]. Over recent years, the energy consumption in MD-based processes for desalination have been considerably cut down by several strategies, resulting in reductions in specific costs. For example, the cost of desalted water from an MD plant (30,000 m^3/d capacity plant) was reduced from 2.2 to 0.66 \$/m^3 by using waste heat [7]. Alternatively, implementation of heat recovery systems have dropped the estimated water cost of a MD plant from 1.17 to 0.64 \$/m^3 when operated with lower grade waste heat [8]. All this makes MD systems competitive against conventional RO plants, which have an estimated cost around 0.8 \$/m^3 water produced. Further improvements in the energy efficiency of MD-based processes, along with an enhanced membrane performance (increasing the flux and reducing membrane wetting), are needed to boost MD technology.

MD membranes can be made from economically affordable and processable polymers. PVDF (polyvinylidene fluoride) offers acceptable hydrophobic properties along with good mechanical and thermal stability and low heat conductivity [10–12]. PVDF membranes are typically prepared by a non-solvent induced phase separation process that yields to an integrally skinned asymmetric structure. This technique allows the fabrication of membranes having a porous structure with high pore connectivity and offers good control of the pore size and membrane porosity. Nevertheless, the performance of PVDF membranes still tends to fall far below PTFE membranes, which are prepared by stretching processes at high temperatures and therefore are more expensive [9,11]. The reason for the lower flux of PVDF membranes is related to their lower hydrophobicity and higher membrane wetting as compared to PTFE [11,12]. Significant research has been carried out towards achieving PVDF membranes that are more economically affordable and have higher fluxes than PTFE membranes. Among all the strategies, the addition of a variety of fillers, including graphene-like materials [13–15], multi-walls carbon nanotubes (MWCNT) [16] and boron nitride nanosheets (BNNs) [17], has led to membranes with enhanced flux without compromising rejection. In particular, the addition of GO and its derivatives (e. g. rGO, APTS-functionalized GO, etc.) have been found very effective for this purpose. For instance, the addition of hydrophilic APTS-GO to the PVDF casting solution enhances the de-mixing process in the coagulation bath during the membrane formation process and leads to membranes with higher porosity as compared to pure PVDF [14]. These membranes were tested for air-gap MD and showed an increase in water flux attributed to the greater membrane porosity. A previous study from our research group involving mixed matrix membranes (MMMs) made of PVDF and rGO with different degrees of reduction demonstrated the influence of the oxygen-containing functional groups within GO in the final properties of membranes such as porosity, membrane contact angle, permeate flux and porosity [13]. The results showed that the improved performance can be due to both hydrophobic and hydrophilic moieties in the nanofillers. Hydrophobic functionalization of GO is particularly attractive since it is typically associated with less pore wetting and higher liquid entering pressure, thus increasing the long-term MD performance [18–20].

Electrospun PVDF membranes with GO functionalized with a few hydrophobic molecules, including polyhedral oligomeric silsesquioxane (POSS) [18], 1 H, 1 H, 2 H, 2 H-perfluorooctyltriethoxysilane (PFOTS) [19] and ocatadecylaime (ODA) [20], have been reported. The above-mentioned molecules possess numerous nonpolar functionalities that barely interact with water molecules; for instance, C-C bonds in ODA and C-F bonds in PFOTS. The addition of these nanofillers to the membrane not only increases its hydrophobicity, but also affects to the diameter of the nanofibers created controlling the porosity of the electrospun nanofibrous membranes. Electrospun membranes have higher water permeance as compared to flat sheet phase inversion membranes due to more favorable membrane properties for water vapor transport. Electrospun membranes consist of a network of interconnected fibers, which results in highly porous structures with very rough surfaces. This high membrane roughness together with the use of hydrophobic polymers leads to highly hydrophobic membranes. The combination of high porosity and high hydrophobicity makes them unbeatable in terms of membrane performance by phase inversion membranes. However, the incorporation of electrospun membranes to the market has been limited by several issues [18,21–23]: i) they often suffer from insufficient mechanical stability, ii) there are not reliable data on long-term operation, and iii) their scalability and cost-effectiveness are questionable. On the contrary, phase inversion is a mature membrane fabrication technology that is already consolidated in the market (e.g. ultrafiltration, nanofiltration, reverse osmosis, and gas separation membranes). This sort of membrane is highly scalable, shows sufficient mechanical stability, their pore size and porosity can be controlled during the membrane fabrication process, and offers satisfactory and reliable long-term performance. Therefore, despite their poorer performance against electrospun membranes, phase inversion flat sheet membranes are still the most reliable alternative to replace conventionally used PTFE membranes.

In this study we compare the performance of phase inversion flat sheet PVDF-based MMMs containing two types of hydrophobic GO fillers: i) octylamine-functionalized reduced GO (OA-rGO), and ii) perfluorooctylamine-functionalized reduced GO (PFOA-rGO). OA-rGO, with long alkyl chains, is expected to offer additional hydrophobicity, whereas PFOA-rGO could offer better compatibility with the fluorinated PVDF polymeric chains due to the presence of inert C-F bonds in the perfluorooctyl chain. Both types of MMMs have been characterized using SEM, contact angle and porosity measurements and studied for treatment of salty water using an air-gap MD (AGMD) configuration.

2. Experimental

2.1. Materials

The following chemicals were used for the preparation of functionalized GO: graphite powder form Nature Graphit GmbH (Germany), hydrogen peroxide (H_2O_2, 30%) and sulfuric acid (H_2SO_4, 98%) from Fisher Chemicals (UK), potassium permanganate ($KMnO_4$, 99%) from Alfa Aesar (UK), nitric acid (HNO_3, 68%), hydrochloric acid (HCl, 37%), octylamine (OA), 1 H,1 H-perfluorooctylamine (PFOA), N,N′-dicyclohexylcarbodiimide (DCC), tetrahydrofuran (THF) and ascorbic acid from Sigma Aldrich (UK).

For the preparation of the polymer membranes, PVDF powder (molecular weight of 534,000 g mol^{-1}) and n,n-dimethylformamide (DMF) were purchased from Sigma-Aldrich. Nonwoven fabric (Viledon Novatexx-2471) was purchased from Freudenberg Filtration Technologies (UK). The coagulation bath contained deionized (DI) water with a resistivity of 18 MΩ cm that was produced by a Milli-Q integral system (Merck Millipore, Ireland). NaCl was purchased from Acros (Belgium).

2.2. Synthesis of graphene oxide and functionalized graphene oxide

GO was prepared according to a modified Hummer's method reported elsewhere [24]. GO was chemically functionalized with the hydrophobic organic molecules OA and PFOA, following the steps that are shown in Fig. 1a. 50 mg of GO and 6.5 mg of DCC were dispersed in 47.5 ml of THF by sonication for 30 min and mechanical stirring for 24 h. Separately, 0.25 mmol of the functionalization agent (i.e. 32.3 mg of OA or 99.8 mg of PFOA) was dissolved in 2.5 ml of THF with the aid of magnetic stirring. The homogeneous GO dispersion was sonicated again for 30 min, transferred to a round bottom flask and heated up to 60 ºC. The THF solution containing the functionalization agent was slowly added to the GO dispersion under magnetic stirring and refluxed for 12 h. After that, the product was filtered using filter paper, washed with abundant THF and DMF and re-dispersed in 50 ml of DMF. 350 mg of ascorbic acid were added to the functionalized-GO dispersion and the mixture was decantated into a round bottom flask where it was reacted at 90 ºC for 4 h under magnetic stirring. The dispersion was then filtered

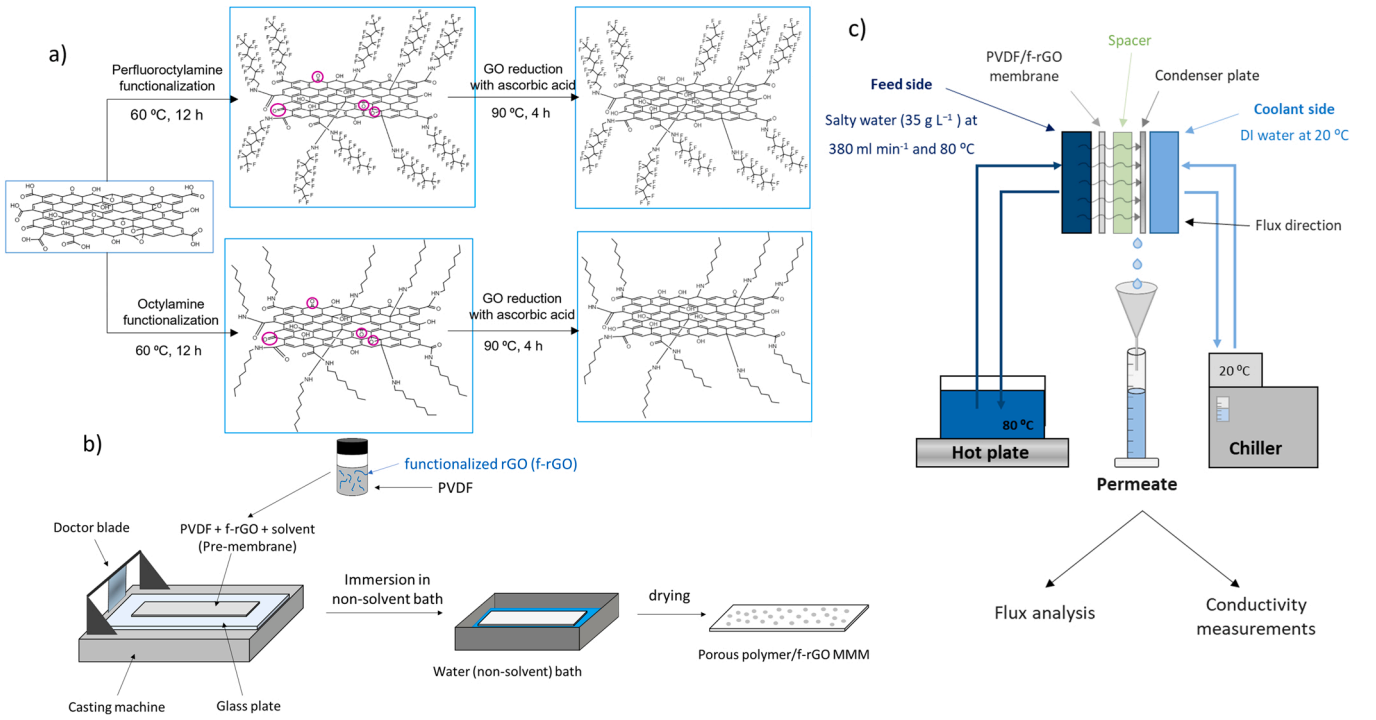

Fig. 1. Synthesis steps for the GO functionalization with octylamine (OA) and perfluorooctylamine (PFOA) and subsequent reduction (resulting solids labeled OA-rGO and PFOA-rGO) (a), PVDF/functionalized-rGO membrane formation process (b) and experimental AGMD setup (c).

and washed with DMF until a colorless solution was found in the filtrate that indicated that most of the ascorbic acid has been removed. The resulting powder was re-dispersed in DMF by sonication for 1 h, filtered over a PTFE filter and washed with DMF.

2.3. Characterization techniques of graphene oxide and functionalized graphene oxide

The chemical composition of GO and functionalized GO was assessed using Fourier-transform infrared spectroscopy (FT-IR) and X-ray photoelectron spectroscopy (XPS). For the ATR-FT-IR measurements an Alpha-P FT-IR spectrometer with a germanium crystal (Bruker, UK) was used with spectra acquired in the range 800–4000 cm^{-1}. XPS measurements were conducted using an Axis Ultra spectrometer (Kratos Analytical Limited, Manchester, UK) having a monochromatic Al Kα source (1486.7 eV) and high resolution XPS spectra were studied using CasaXPS software.

2.4. Membrane fabrication

The membrane fabrication process is depicted in Fig. 1b. PVDF membranes were prepared by a phase inversion process using casting solutions with a polymer concentration of 14 wt% in DMF. Fillers OA-rGO or PFOA-rGO nanofillers were added into the casting solutions to obtain final concentrations of the filler in the prepared membranes of 0.2–1 wt% (exact amounts are shown in Table 1). For the phase inversion process, a piece of non-woven fabric was coated with the prepared dope solutions using an automatic film applicator (Sheen) equipped with a doctor blade. The height of the doctor blade was set at 200 μm and a coating velocity of 0.05 m s^{-1} was used. Immediately after casting, the non-woven fabric coated with the dope solution was immersed in the coagulation bath containing deionized water at room temperature to allow phase separation and polymer solidification. The resulting membranes were left in the coagulation bath for 5 min before being transferred to another DI water bath. After 24 h, the membranes were taken out from the water and left to dry in a fume cupboard for 48 h. As seen in Table 1, the resulting MMMs were denoted by the same name as the type of nanofiller used; for instance, 0.2% OA-rGO corresponds to MMMs containing 0.2 wt% of OA-rGO nanofiller and 98.8 wt% PVDF.

Table 1
Composition of the PVDF casting solutions used for the preparation of the MMMs.

Membrane code (%loading+filler)	PVDF (g)	DMF (g)	Filler (mg)
PVDF	1.54	9.44	-
0.2% OA-rGO	1.54	9.44	3.1
0.5% OA-rGO	1.54	9.44	7.7
0.7% OA-rGO	1.54	9.44	10.8
1% OA-rGO	1.54	9.44	15.4
0.2% PFOA-rGO	1.54	9.44	3.1
0.5% PFOA-rGO	1.54	9.44	7.7
0.7% PFOA-rGO	1.54	9.44	10.8
1% PFOA-rGO	1.54	9.44	15.4

2.5. Membrane characterization

Top-view and cross-sectional images of the membranes were acquired using a scanning electron microscope (SEM), FEI Quanta 650 FEG-SEM microscope (FEI, USA) at a voltage of 20 KV. Cross-section specimens were immersed in liquid N_2 for 10 s and fracture inside of the liquid to render a cleaner exposed section. All samples were sputter coated with platinum (MTM 10 Thickness Monitor, Cressington, USA) prior to imaging.

Attenuated total reflectance-Fourier-transform infrared spectroscopy (ATR-FTIR) was conducted using an iDS Nicolet iS5 spectrometer (Thermo Scientific, UK) with a Ge crystal as a background within a wavenumber range of 1600–700 cm^{-1} and a step size of 0.5 cm^{-1}. Prior to carrying out AFT-FTIR measurements, the membranes were left to dry inside of the fume hood for 24 h at room temperature to avoid the presence of fictitious peaks in the spectra that may arise due to the presence of water trapped within the membranes [25].

Contact angle measurements via Sessile Drop Method were

performed to investigate the hydrophobicity of the membranes. A 10 μL droplet was deposited on the surface of the membrane and then imaged using a Digilife digital microscope from KKMoon. For each membrane, the contact angle value reported corresponds to the average of five measurements.

The porosity (ε) of the prepared membranes was evaluated by using the gravimetric method [26,27]. For each membrane, squares pieces of approximately 1 cm × 1 cm were weighed (W_d) and then immersed in ethanol at room temperature. After 1 h, the pieces were removed from the ethanol, the excess solvent on the membrane's surface was gently wiped off with tissue paper, and then each piece was weighed again (W_w). For each membrane sample (e.g. 0.2% OA-rGO), three pieces were measured and the average value is reported. The porosity was calculated using Eq. (1) [28]:

$$\varepsilon = \frac{\frac{W_w - W_d}{\rho_e}}{\frac{W_w - W_d}{\rho_e} + \frac{W_d}{\rho_p}} \times 100 \quad (1)$$

where W_w and W_d correspond to the weight of the wet and dry membrane, respectively, and ρ_e (789 kg m^{-3}) and ρ_p (1740 kg m^{-3}) are the densities of ethanol and polymer, respectively (source: Sigma Aldrich).

Atomic Force Microscopy (AFM) measurements were carried out using a Bruker MultiMode 5 scanning probe microscope in tapping mode with a scan rate of 1 Hz and an approximate amplitude of 250 mV. The following roughness parameters were calculated using Gwyddion, a free software for scanning probe microscopy data visualization and analysis: average roughness (Ra) and Root mean square (RMS). A scanning area of 5 × 5 μm was used to analyze the roughness parameters.

Capillary flow porometry was conducted at room temperature using a Porolux 1000 (Porometer, Belgium) connected to a N_2 gas line. The membrane samples were immersed in POREFIL 125 (surface tension of 15.88 ± 0.03 mN m^{-1}) for 5 min prior to analysis. The bubble point pore size (BP) and mean flow pore size (MFP) were calculated using the dry/wet method as explained elsewhere [14].

Liquid entry pressure (LEP) measurements were acquired at room temperature using an aqueous solution of NaCl (35 g L^{-1}) and a stirred dead-end filtration cell (Sterlitech HP4750) connected to a nitrogen gas cylinder for pressurization up to 10 bar. The pressure was gradually raised stepwise until the first drop of solution eluted. Three samples for each membrane code were measured and then averaged.

2.6. Performance in AGMD

The scheme in Fig. 1c represents the air gap membrane distillation (AGMD) setup employed for measuring the MD performance of the membranes. Membranes were placed in the module along with rubber gaskets, a spacer, a perforated plastic support disk and a metallic condenser plate. The spacer allows for an air gap with a width of 3 mm since this has been found to be the optimum value [29]. A membrane with an area of 28.27 cm^2 was used in this study, nonetheless, due to the perforated membrane support, the effective membrane area exposed to the condenser plate was 7.16 cm^2. However, the full membrane area, i.e. 28.27 cm^2, was used in the flux calculations since this is the area exposed to the feed solution. The feed was an aqueous NaCl solution of 35 g L^{-1} at 80 °C, which was re-circulated at a flow rate of 385 ± 5 ml min^{-1} using a pump. On the permeate side, the condenser plate was maintained at 20 °C due to water circulation using a Julabo F12-ED chiller. The amount of permeate collected was weighed to calculate the membrane flux, taking readings each 15 min up to 2 h. To assess the reproducibility of the setup, three coupons were tested for each membrane. The permeate flux, J (L m^{-2} h^{-1}, LMH), was calculated using Eq. (2):

$$J = \frac{V_p}{tA} \quad (2)$$

where V_p (L) is the volume of the permeate collected at time t, t (h) is the time of the experiment and A (cm^2) is the membrane area. Salt rejection (%) was calculated using Eq. (3):

$$\text{Salt Rejection} = \left(1 - \frac{C_p}{C_f}\right) x100 \quad (3)$$

where C_p (μS cm^{-1}) and C_f (μS cm^{-1}) are the conductivities of permeate and feed solutions, respectively.

3. Results and discussion

3.1. Characterization of GO and OA-functionalized GO and PFOA-functionalized GO

The functionalization of GO with OA and PFOA was assessed by FT-IR prior to the reduction of GO with ascorbic acid. The FT-IR spectra of GO and the functionalized GO are shown in Fig. 2a, and some differences are observed. A new band at around 1300 cm^{-1} in both functionalized GO samples appear as a result of C-N stretching vibrations. However, this band is more intense in the spectrum of OA-GO as compared to PFOA-GO due to the contribution of C-H stretching vibrations from the alkyl chain in OA that appears at very similar wavenumbers to C-N vibrations. The functionalization also leads to the broadening and decrease in intensity of the GO's sharp peak at 1600 cm^{-1} that corresponds to C═C vibrations. This is due to overlap with O═C-N stretching bonding vibrations (commonly ~1500–1700 cm^{-1}) [30–32]. In addition, amide formation leads to an intensity decrease of the peak at 1720 cm^{-1} attributed to C═O groups. Furthermore, the use of different functionalizing agents gives rise to few discrepancies between both spectra. The FT-IR spectrum of OA-GO shows the presence of CH_2 groups at 2800–2900 cm^{-1} [30,32], whereas the spectrum of PFOA-GO reveals characteristic C-F vibrations at 1100 (CF_3 stretching), 1140 (symmetrical stretching CF_2) and 1200 cm^{-1} (asymmetrical stretching CF_2) [33–36].

After functionalization of GO, both OA-GO and PFOA-GO were reduced using ascorbic acid. XPS was used to investigate the functionalization of GO (prior to treatment with the reducing agent, i.e. OA-GO and PFOA-GO), and the material obtained after the reduction process (i.e. OA-rGO and PFOA-rGO). C 1 s high resolution spectra of all the materials are presented in Fig. 2b-f and confirm the chemical reaction proposed in Fig. 1a. The introduction of CH_2 and CH_3 present in the alkyl chain of OA increases the contribution of the C-C peak in the C 1 s high resolution spectrum of OA-GO (Fig. 2c) as compared to that of GO (Fig. 2b) [37,38]. However, in the case of PFOA-GO (Fig. 2d), the addition of perfluoroalkyl chain introduces two new peaks at 291.3 and 293.4 eV corresponding to CF_2 and CF_3, respectively [39–41]. In both OA-GO and PFOA-GO spectra, the peak of C-N overlaps with that of C-O [38], and the peak around 286.4–284.7 eV is assigned to both C-O and C-N [42–44]. This slightly shifts the peak position towards lower energies as compared to the C-O peak in GO. Likewise, the positions of the peaks assigned to C═O and N-C═O in both spectra (at 288.2 and 287.8 eV in the OA-GO and PFOA-GO spectra, respectively), appear at lower energies as compared to the C═O peak at 288.8 eV in the GO spectra. The reduction of both functionalized GO materials (i.e. OA-rGO and PFOA-rGO, Fig. 2e and f, respectively) results in a decrease in the C-O and C═O peaks as compared to its unreduced counterparts OA-GO and PFOA-GO. In addition, the reduction process leads to a partial restore of the aromatic structure of GO, which is observed in the C 1 s high resolution XPS spectra as an increase in the area of the C═C bonds and a decrease in the area of the C-C bonds [45]. In the case of OA-rGO, the peak corresponding to C-C bonds is still perceptible due to the presence of alkyl chains. However, in the spectrum of PFOA-rGO, the C-C peak is absent since the contribution of the C═C is much higher than that of C-C, and then the C-C peak cannot be distinguished.

High resolution spectra of N 1 s, O 1 s and F 1 s are presented in the

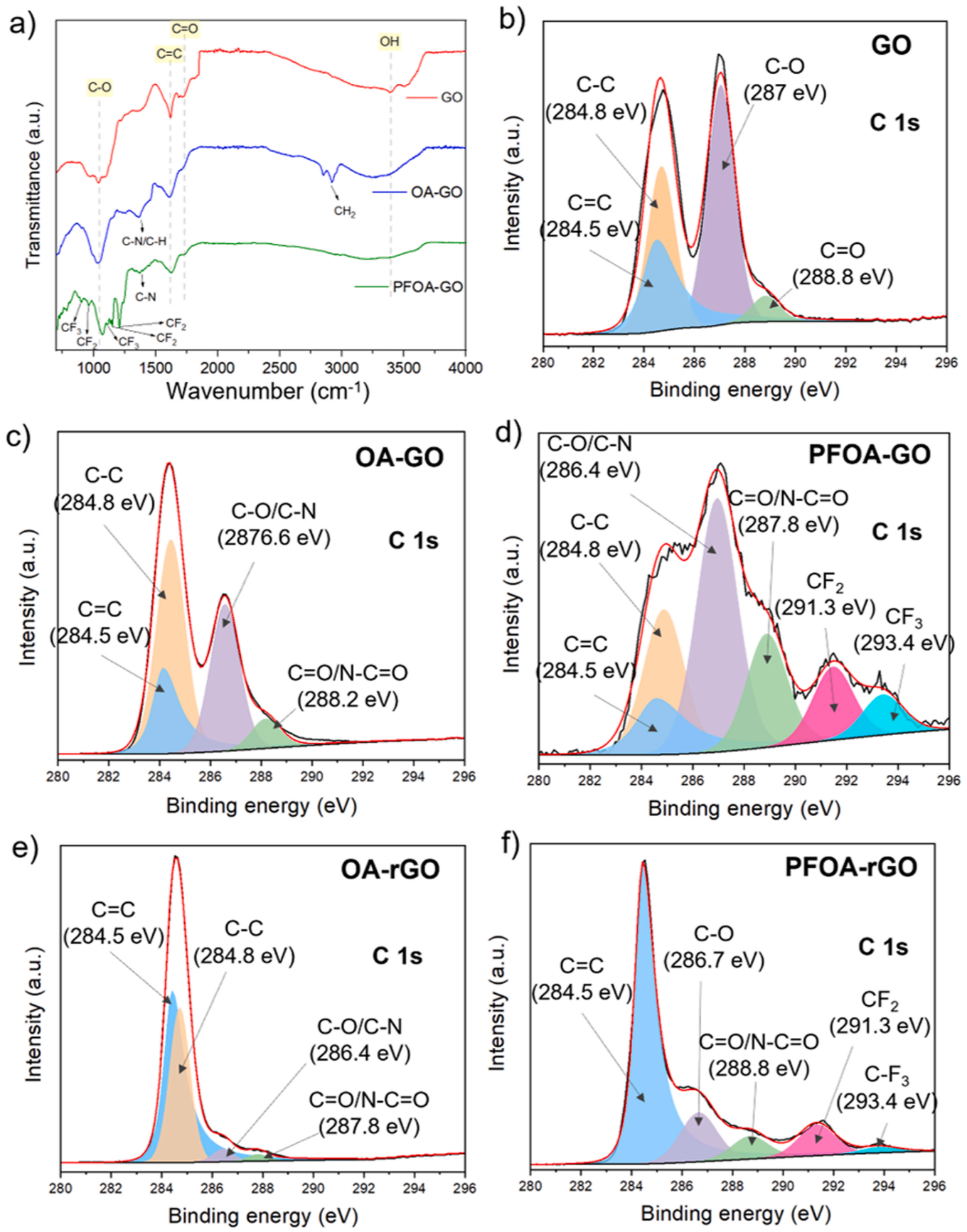

Fig. 2. FT-IR of GO, OA-GO, PFOA-GO (a) and C1s high resolution XPS spectra of GO (b), OA-GO (c), PFOA-GO (d), OA-rGO (e) and PFOA-rGO (f). In all the XPS spectra, the red line corresponds to the fitted spectrum and the black line to the measured XPS signal.

supporting information (Fig. S1). The peaks attributed to N-CH and N-C═O in the N 1 s high resolution XPS spectra of both functionalized reduced GO confirm the presence of OA and PFOA after the reaction of GO [42,46,47]. The presence of CF_2 and CF_3 are also depicted in the F 1 s high resolution spectrum of PFOA-rGO [39–41].

The degree of functionalization was calculated from the C 1 s, O 1 s, N 1 s and F 1 s high resolution XPS spectra of all the material synthesized and is shown in the supporting information (Table S1) along with the atomic ratio of each element.

3.2. Membrane characterization

A three-phase diagram of PVDF membrane formation using DMF as solvent and water as non-solvent is shown in Fig. 3a. Mohsenpour et al. [48] studied the addition of GO and rGO to PVDF/DMF casting solutions and their effect on the thermodynamic stability of the solution [48]. Both theoretical and experimental studies revealed that the addition of any of the nanofillers, hydrophilic GO or hydrophobic rGO, shifts the binodal line towards the PVDF-DMF axis which means that less water is required to precipitate the casting solution, i.e. thermodynamic instability increases. In terms of membrane morphology, an increase in thermodynamically stability leads to faster solvent/nonsolvent de-mixing rate, and then higher porosity and larger and more abundant presence of finger-like voids [48,49].

The membrane porosity was calculated using the gravimetric method described in the methodology section. As seen in Fig. 3b, the presence of nanofillers results in membranes with higher porosities. This has also been shown for other PVDF-based MMMs containing graphene-like nanofillers such as GO [14,48], APTS-GO [14] and rGO [13,48]. As abovementioned, the addition of graphene-like nanofillers increases the thermodynamic instability of the casting solution and promotes faster de-mixing process [13,14,48,50]. In all these studies [13,14,48], the porosity increased with the loading of nanofiller until a maximum value at an optimum loading, and then decreased. For both OA-rGO and PFOA-rGO in this study, the loading that leads to membranes with the highest porosity is 0.5 wt%, similar to that observed for PVDF MMMs containing rGO [13]. The existence of a crossover point above which the porosity starts decreasing has been attributed to an increase in viscosity of the PVDF/nanofiller casting solutions as the loading of nanofiller increases, which hinders the de-mixing process in the coagulation step

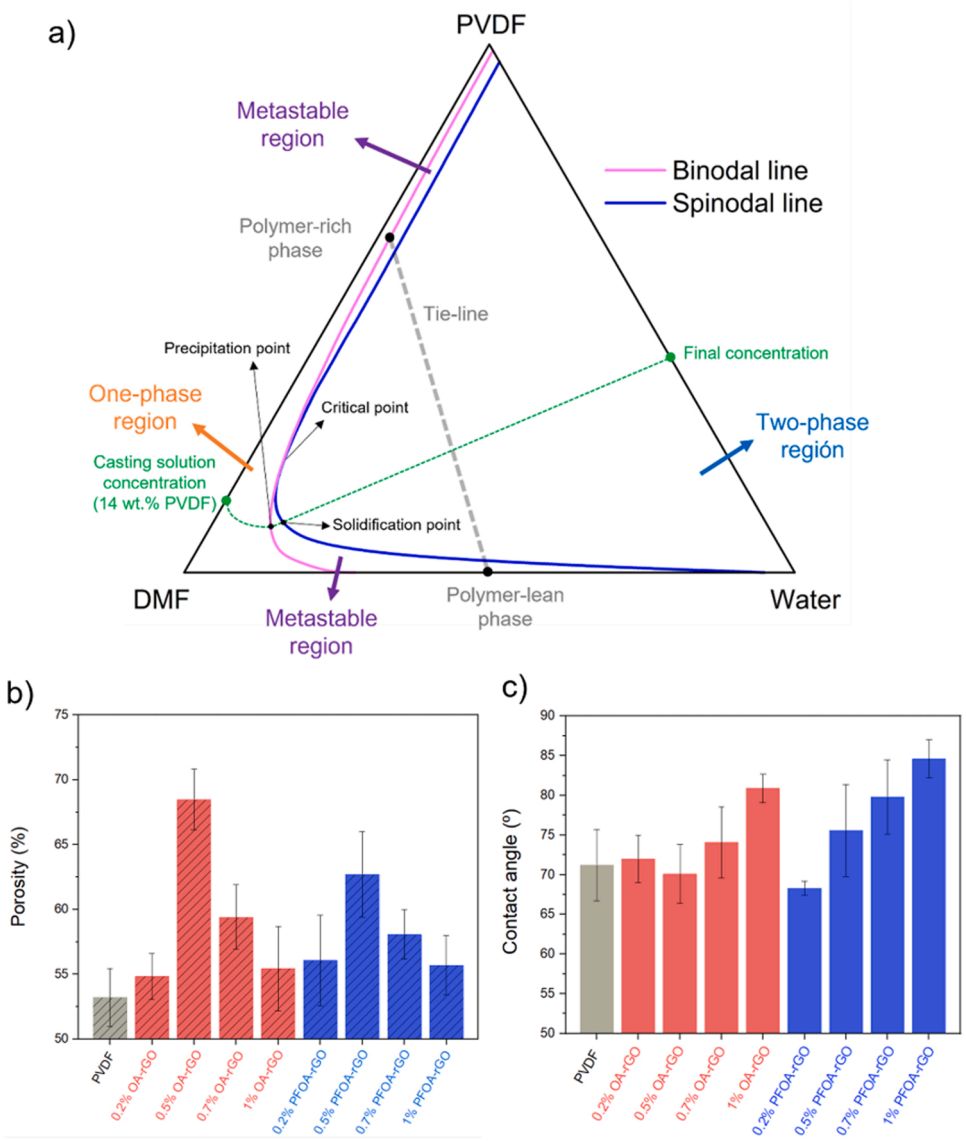

Fig. 3. Schematic of a three-phase diagram using a casting solution of 14 wt% PVDF in DMF and water as non-solvent (a), porosity (b), and contact angle data (c) of pure PVDF and MMMs containing OA-rGO and PFOA-rGO. In Fig. 3a, binodal and spinodal lines have been constructed according to data obtained from Mohsenpour et al. [48].

resulting in membranes with lower porosity [13,48].

Contact angle measurements suggest a general trend of increased hydrophobic character of the membrane surface with the incorporation of OA-rGO and PFOA-rGO nanofillers. Fig. 3c shows the highest values of water contact angle at 1% OA-rGO (80.9º) and 1% PFOA-rGO (84.6º). However, due to the observed relatively large standard deviations for the contact angle measurements at filler loadings of up to 0.7 wt%, it is difficult to see a clear effect in this lower range. It is worth noting that the addition of the hydrophobic nanoparticles has two overlapping effects, i) the higher the nanofillers loading, the higher the hydrophobic nature of the membrane surface and higher the water contact angle should be, and ii) the influence of nanofillers in the membrane porosity, with higher porosities leading to lower contact angle due to higher water penetration in the membrane. Thus, it can only be concluded that despite the increase in porosity for all the MMMs, the highest loading of 1 wt% leads to a significant increase in water contact angle for the two types of functionalized rGO fillers. When comparing both types of nanofillers, it is observed that the addition of the GO with perfluoroalkyl chains (PFOA-rGO) leads to more hydrophobic surfaces, which is related to the higher hydrophobicity of C-F moieties as compared to C-H [51, 52]. The hydrophobicity of the perfluoroalkyl chain arises from the strong electronegativity of fluorine atoms that makes the electrons at the outer shell of the fluorine atoms inert, and then exhibit very limited intermolecular interactions with polar heteroatom solvent molecules such as water [52]. In addition, perfluorooctyl chains are larger than octyl chains, which results in a larger free-energy penalty for molecule hydration, considered as the main reason of the higher hydrophobicity of perfluoroalkanes as compared to alkanes [51]. Several GO-like materials with a variety of chemical functionalizations have been used as nanofillers in PVDF membranes. It has been demonstrated that the chemistry of the GO nanofiller alters the contact angle. APTS-GO having both hydrophilic and hydrophobic moieties increased the contact angle of PVDF membranes (from 70.7º to 77.6º) [14], whereas GO and rGO nanofillers with different degrees of reduction led to a reduced contact angle as compared to PVDF [13]. Electrospun nanofibrous PVDF-based MMMs have also been prepared using hydrophobic additives, such as PFOTS-GO [19] and ODA-rGO [20], which have demonstrated a strong ability to increase the membrane contact angle similar to that shown in Fig. 3c.

The surface of all membranes was analyzed by SEM. A selection of SEM images is shown in Fig. 4, and more images (0.2% OA-rGO and 0.2% PFOA-rGO membranes) can be found in the supporting information (Fig. S2). MMMs containing 0.5% OA-rGO and 0.5% PFOA-rGO have larger pore sizes than other MMMs and pure PVDF, which is in good agreement with the porosity measurements previously discussed. According to SEM images, the biggest pore size for PVDF is around of 300 nm, whereas for 0.5% OA-GO and 0.5% PFOA-rGO are around 370 and 350 nm, respectively. At higher loadings of nanofillers, e.g. 0.7% and 1% OA-rGO, the increased viscosity of the casting solution inhibits the solution de-mixing process due to higher kinetic hindrance resulting in denser skin layers and pore sizes similar to those of pure PVDF.

Cross-sectional SEM images of PVDF and (OA-rGO)-containing membranes are shown in Fig. 5. All membranes show an asymmetric structure having finger-like pores in the intermediate layer with several sponge-like pores underneath. The skin layer on top is particularly thin due to the fast de-mixing process between DMF and water at this polymer loading in the dope solution. This results in the presence of wide pores in the membrane surface and a very thin top layer where the formation of a dense polymer layer is prohibited. The addition of the nanofiller barely alters the morphology of the membranes. As previously discussed, the addition of OA-rGO and PFOA-rGO nanofillers increases the membrane porosity by increasing the membrane pore size, but do not suggest the formation of notoriously bigger pores in the intermediate layer of MMMs as compared to pure PVDF. Cross-sectional SEM images of membranes containing PFOA-rGO nanofillers are shown in the supporting information (Fig. S3) and the same conclusions can be inferred, the addition of the perfluoro-functionalized nanofiller does not lead to a significant change in the membrane morphology.

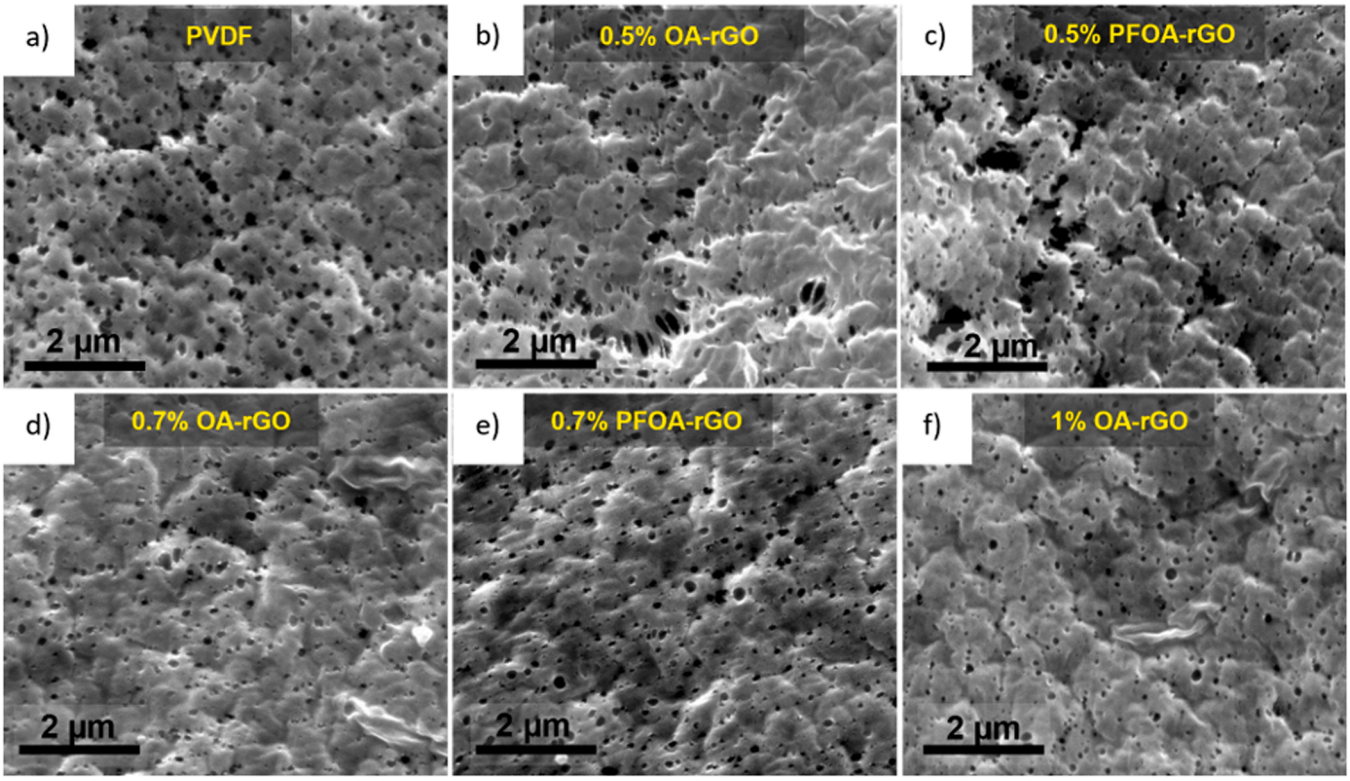

Fig. 4. SEM surface images of PVDF (a) and MMMs having 0.5% OA-rGO (b), 0.5% PFOA-rGO (c), 0.7% OA-rGO (d), 0.7% PFOA-rGO (e) and 1% OA-rGO. A magnification of 20,000, a spot size of 3, and a voltage of 20 kV were used for the acquisition of all images.

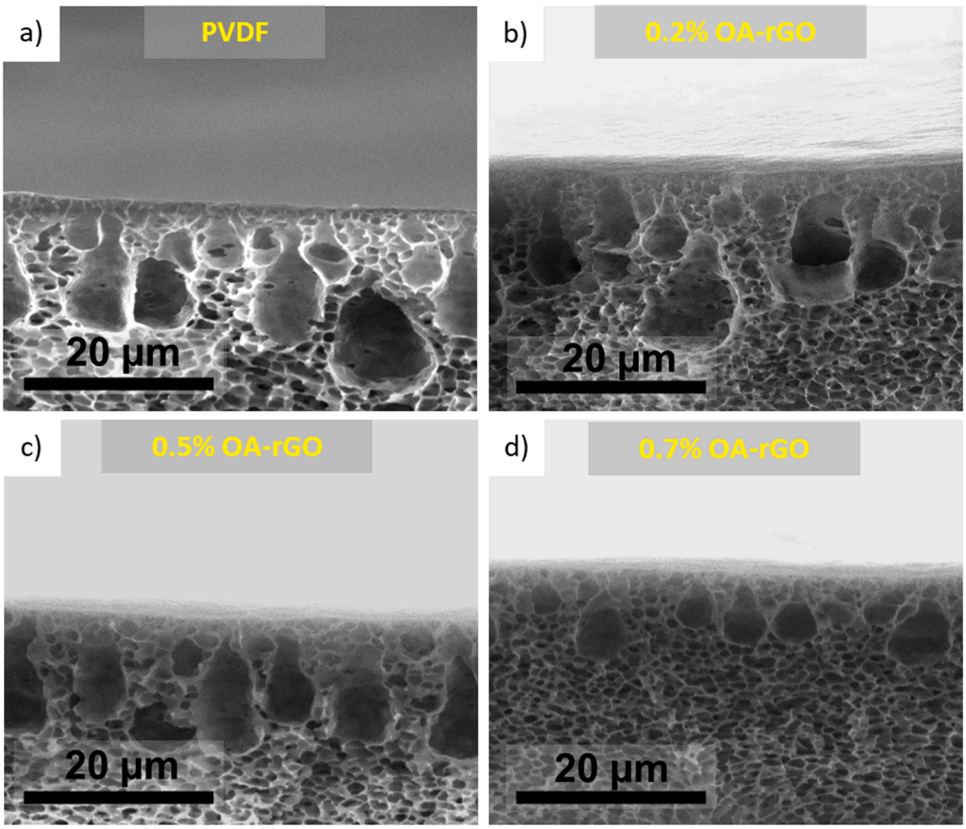

Fig. 5. Cross-sectional SEM images of PVDF (a) and MMMs having 0.2% OA-rGO (b), 0.5% OA-rGO (c) and 0.7% OA-rGO. A magnification of 3000, a spot size of 3, and a voltage of 20 (for a and b) and 15 kV (for c and d) were used for the acquisition of all images.

Fig. 6 shows the FTIR spectra of PVDF and both sort of MMMs. Characteristic peaks of PVDF are observed, including backbone functional groups (CF_2 bounds at 1176 cm^{-1} and CH_2 at 1400 cm^{-1}), α-phase (at 762, 796, 976, 1380, 1400, and 1423 cm^{-1}), and β-phase (at 840, 1074, and 1274 cm^{-1}) [14,53,54]. Subtle differences are observed in the FTIR spectra of PVDF and MMMs containing OA-rGO and PFOA-rGO. A small peak around 1233 cm^{-1} is observed in the spectra corresponding to 0.5% and 0.7% PFOA-rGO (indicated by a pale-yellow inset) which arises from CF_2 vibration bands characteristic of the perfluoroalkane-functionalized nanofiller. This has been previously observed in MMMs containing PVDF and perfluoroalkane-GO nanofillers [19] and, similar to that shown in Fig. 6, this feature was only noticeable above a certain nanofiller loading due to a strong overlap with the polymer absorption bands. Another significant difference of PFOA-rGO-based MMMs with PVDF (highlighted by a pale-blue inset) is the decrease in the α-phase (740 and 976 cm^{-1}) of PVDF chains and the subsequent increase of the β-phase (840 cm^{-1}) [55–58]. This crystalline phase transition can be attributed to strong intermolecular forces between the polymer chain (fluorinated polymer) and the nanofiller (fluorinated functionalization) that triggers a phase rearrangement of the PVDF chains surrounding the nanofiller from an α- to a β-conformation [56,57]. As previously mentioned, these features are more noticeable at the two highest loadings of PFOA-rGO, i.e. 0.5% and 0.7%. MMMs containing OA-rGO (no fluorinated functionalization) do not

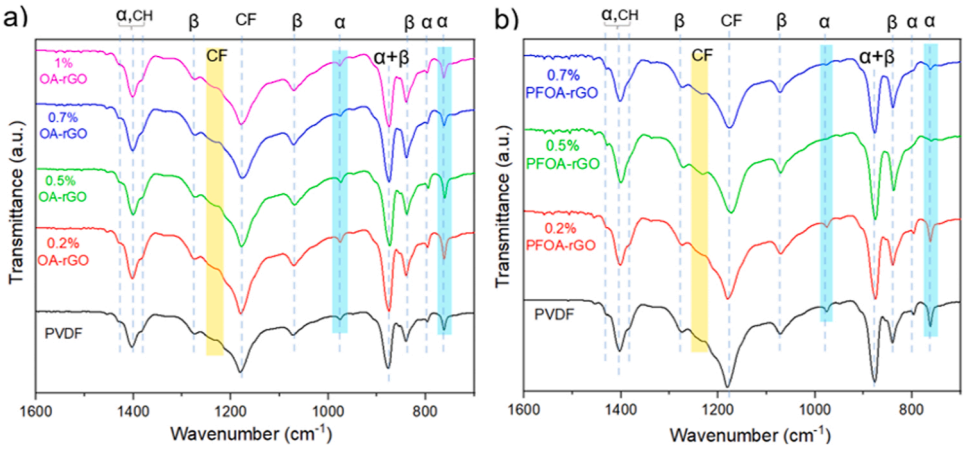

Fig. 6. FT-IR spectra of pure PVDF and MMMs containing OA-rGO (a) and PFOA-rGO (b). The blue inset indicates the peaks corresponding to α-phase and β-phase, whereas the pale-yellow inset highlights the position corresponding to the characteristic vibration band of CF_2 groups.

show any noticeable change in the intensity of the bands at 740 and 976 cm^{-1} (corresponding to α-phase). This suggests that octylamine-functionalized rGO does not interacts with PVDF chains, or it does in a minor degree as compared to PFOA-GO, and then phase rearrangement of the PVDF is not observed for MMMs containing OA-rGO although it is clear for MMMs containing PFOA-rGO.

AFM measurements were conducted to study the roughness of the prepared membranes by means of the Ra and RMS parameters (Fig. 7). The addition of 2D nanofiller has been found to influence the membrane roughness due to the following effects: i) individual 2D nanosheets embedded in the polymer matrix which are located near the membrane surface leads to flatter morphologies, and then lower roughness parameters, ii) agglomeration of 2D nanosheets disrupt polymer packing around the nanofiller and significantly increases the surface roughness, and iii) rapid de-mixing, due to an increased thermodynamic instability, can also be blamed for presence of uneven surfaces. It is then expected that the loading of the nanofiller plays a decisive role in the membrane roughness properties. Fig. 7 reveals that both 0.5% and 0.7% OA-rGO possess rougher surfaces as compared to PVDF. This increase in surface roughness is attributed to nanofiller agglomeration [13,14,59]. However, when PFOA-rGO are employed at loadings of 0.5% and 0.7%, the roughness parameters decrease with the filler loading remaining at lower RMS and Ra values than pure PVDF. According to FITR analysis, the incorporation of PFOA-rGO nanofillers results in a phase transition of PVDF due to intermolecular forces between the nanofiller and the polymer chains, i.e. between perfluoroalkyl amine molecules in PFOA-rGO and perfluoroalkyl moieties in PVDF. These intermolecular forces aid in stabilizing the nanofiller within the polymer matrix and preventing them from agglomeration, which explains why the roughness parameters of PFOA-rGO membranes decreases as the loading of nanofiller increases.

Water LEP was analyzed for selected membranes and results are displayed in Fig. 8. PVDF shows a LEP of 5.4 bar, similar to those reported in the literature [60–62]. When OA-rGO and PFOA-rGO are added, the LEP increases with the loading of the nanofiller due to an increase in hydrophobicity. The membrane with the highest contact angle amongst those selected for LEP experiments, i.e. 0.7% PFOA-rGO, shows the highest LEP value of 7.1 bar. Top-view SEM images (Fig. 4) suggest the existence of slightly larger pores in 0.5% OA-rGO and 0.5% PFOA-rGO (largest pore around 370 and 350 nm, respectively), as compared to PVDF (~ 300 nm), which could decrease the LEP of these membranes. However, LEP analysis reveals that the increase in hydrophobicity dominates the surface properties and results in an increase of LEP values for all the MMMs.

Capillary flow porometry measurements of PVDF, 0.7% OA-rGO and 0.7% PFOA-rGO were carried out to investigate the pore size of the membranes. The obtained BP and MPF values are displayed in Table S2 in the supporting information. BP values of both 0.7% OA-rGO and 0.7% PFOA-rGO are 0.45 and 0.28 μm, respectively, which are slightly lower than that of PVDF (0.50 μm). However, both 0.7% OA-rGO and 0.7% PFOA-rGO membranes exhibited higher MFP (0.19 and 0.15 μm, respectively) as compared to PVDF (0.11 μm). These BP and MPF values are similar to reported ones for other PVDF/GO membranes [13,14]. Pore wetting will likely occur in membranes where the pore size is above 1.2 μm [63], which is not the case for membranes prepared in this work.

3.3. AGMD membrane performance

The use of OA-rGO and PFOA-rGO nanofillers significantly improves the MD performance of the membranes in terms of flux with little effect on the salt rejection. As seen in Fig. 9a, all the prepared MMMs, except for 1% OA-rGO, show higher fluxes than pure PVDF membranes. 0.7% PFOA-rGO and 0.7% OA-rGO exhibit the highest pure water fluxes among all MMMs with a flux of 8.8 and 9.1 LMH, respectively, which represent a 76% and an 82% increase as compared to pure PVDF (pure water flux of 5 LMH). The increase in water vapor transport through the MMMs is related to the more hydrophobic surfaces (i.e. less pore wetting and higher water LEP), as well as higher porosities of the MMMs. When comparing MMMs containing the same loading of OA-rGO and PFOA-rGO nanofillers, Fig. 9a shows that both achieve very similar water flux values. According to the previously discussed characterization, PFOA-rGO leads to slightly more hydrophobic membranes, whereas OA-rGO results in slightly more porous membranes. Then, when comparing both nanofillers exists a tradeoff between enhancement in porosity and improvement in the hydrophobic character and none of the nanofillers offers a substantial advantage over each other. During the MD tests, all MMMs achieved very low electrical conductivity in the permeate resulting in rejections of salt above 99.9%, which is considered as excellent salt rejection values (Fig. 9a).

The MMMs reported in this study were compared with those published somewhere else. It can see in Fig. 9b that the use of hydrophobic functionalized GO along with PVDF produces MMMs showing pure water fluxes comparable to other successful MMMs. The use of hydrophobic nanofillers offer some advantages as compared to bare GO [14], rGO [13] or hydrophilic APTS-GO [14] due to the formation of surfaces with higher hydrophobicity, less pore wetting and consequently higher water vapor flux and salt rejections. Recently, this principle of using hydrophobic functionalized GO nanofillers in combination with PVDF was explored through the preparation of electrospun membranes for As removal using air gap MD [18]. In that work it was reported that the addition of hydrophobic POSS-rGO to the PVDF matrix boosted water flux through the membranes, in line with what we have observed when adding OA-rGO and PFOA-rGO. Similar graphene-like materials to those reported in this manuscript, such as PFOTS-GO [19] and ODA-rGO [20], have been also used in combination with PVDF for the formation of electrospun membranes leading to increase in membrane flux [64]. As compared to other non-hydrophobic GO, the MMMs presented in this study exhibit some of the best NaCl rejections among all PVDF/GO-like nanofillers MMMs (Fig. 9b). As aforementioned, using hydrophobic additives reduces the membrane pore wetting hindering the transport of liquid water, which increases the salt rejection and potentially allows for bigger pores. Fig. 9b also includes the performance of a commercial PTFE membrane previously tested in our group using the same MD equipment but an aqueous solution of NaCl and organic dyes as the feed [65]. In comparison with the PTFE, MMMs displayed a slightly lower flux but they have the advantage of being produced using much cheaper materials via a phase inversion process, which is a well-established technique in the membrane manufacturing industry and much more cost effective and less energy intensive than the stretching process commonly used to fabricate PTFE membranes. The superior performance of the PTFE membranes can be explained by their high porosity (around 80%) and high contact angle (105°) [65], as compared to the MMMs shown in this study (55–69% of porosity and contact angle of 69–84.6°). However, the performance of the MMMs presented in this study could still be further improved by following several strategies, which are compatible with the use of graphene nanofillers, such as the use of additives (e.g. water [61], LiCl [66] and polyvinylpyrrolidone [67]), lowering the polymer concentration in the dope solution [68], etc.

Long-term operation was conducted for the best performing membrane (0.7% OA-rGO) with the aim of investigating its robustness under continuous operational conditions. Undesirable effects such as pore wetting compromise the membrane performance. However, the stable water flux and salt rejection values shown by 0.7% OA-rGO membrane (Fig. 10) indicate lack of such phenomenon for the testing period. An initial flux of 9.3 LMH and 99.98% salt rejection were obtained, which were maintained after 162 h of operation (~9 LMH and a rejection of 99.94%).

4. Conclusion

In this study, hydrophobic functionalized of rGO nanofillers were

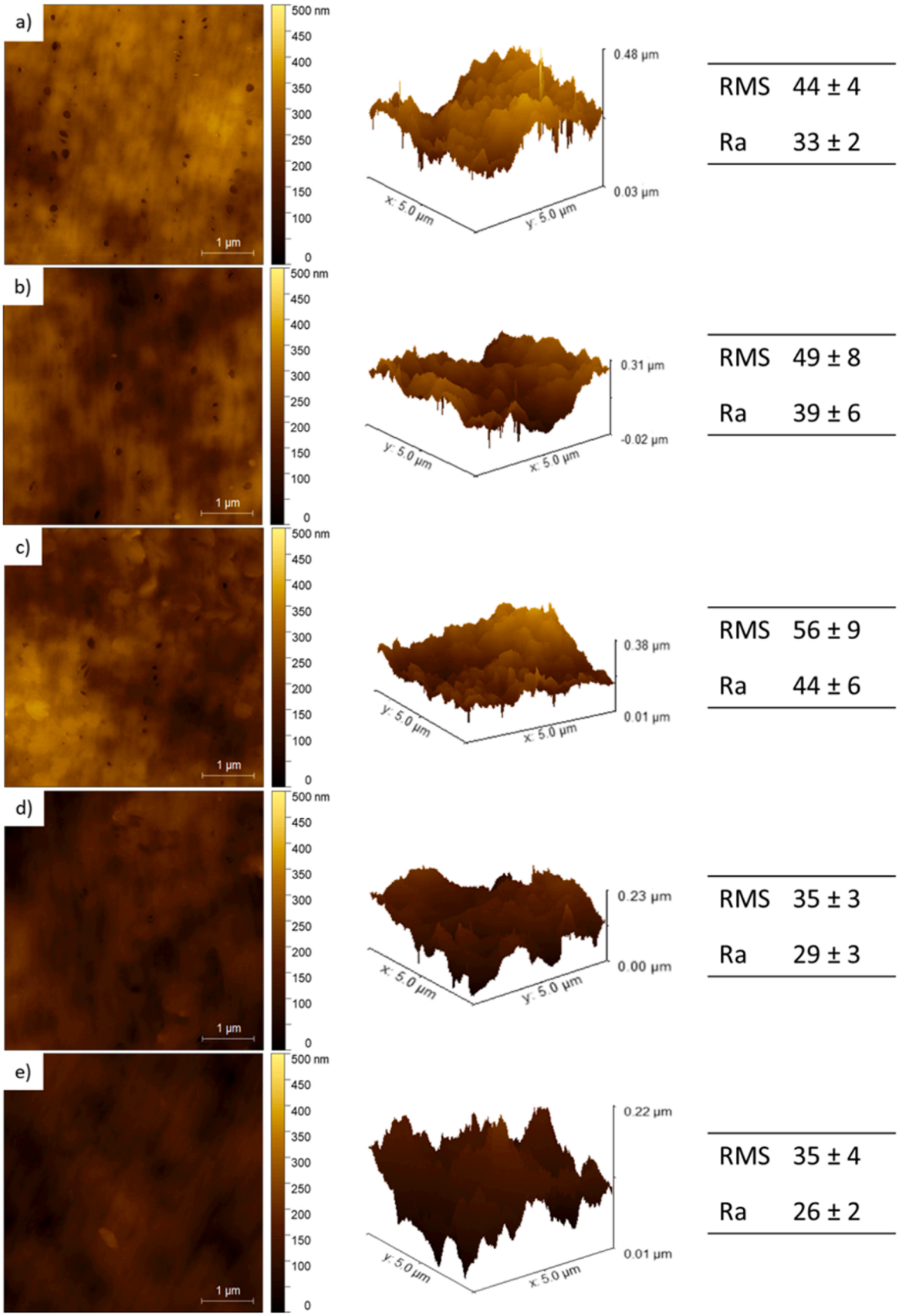

Fig. 7. 2D top-view images, 3D representation, and roughness parameters (RMS and Ra) of PVDF (a), 0.5% OA-rGO (b), 0.7% OA-rGO (c), 0.5% PFOA-rGO (d), and 0.7% PFOA-rGO (e) membranes. All 2D and 3D images have been prepared using the same color scale ranging from 0 to 500 nm.

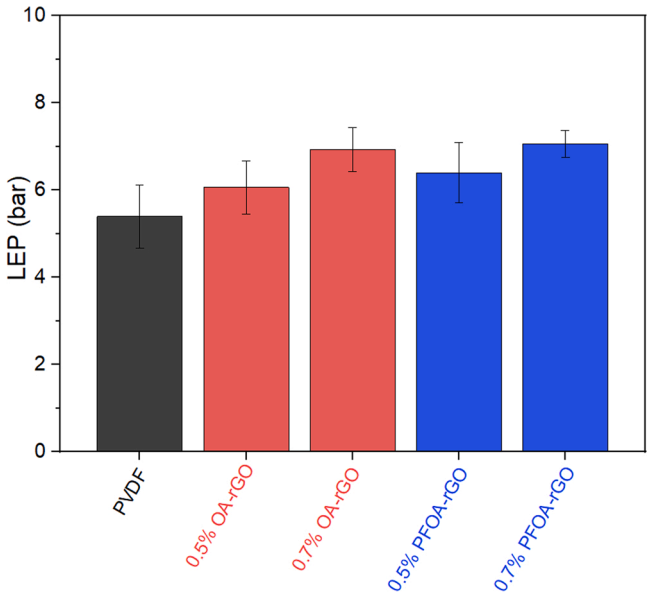

Fig. 8. LEP values of PVDF (a), 0.5% OA-rGO (b), 0.7% OA-rGO (c), 0.5% PFOA-rGO (d), and 0.7% PFOA-rGO (e).

synthesized and used for the preparation of MD membranes. The functionalization of GO with two hydrophobic amine-based agents and their incorporation into PVDF membranes leads to superior water flux and rejection as compared to pure PVDF and other reported PVDF-based MMMs containing GO-like nanofillers. Despite the chemical differences between both functionalization agents (OA and PFOA), both nanofillers yield to very similar membrane performances with the best performing membranes achieving water flux of 8.8 and 9.1 LMH for 0.7% PFOA-rGO and 0.7% OA-rGO, respectively. These water fluxes represent a flux increase of 76% and 82% for 0.7% PFOA-rGO and 0.7% OA-rGO, respectively, as compared to the pure PVDF membranes (flux of 5 LMH). The salt rejection was 99.9% for both 0.7% OA-rGO and 0.7% PFOA-rGO (salt conductivity in the permeate of 14.5 and 16.6 μS cm^{-1} for 0.7% OA-rGO and 0.7% PFOA-rGO, respectively). The enhanced water flux is attributed to the higher membrane hydrophobicity along with higher porosities of the MMMs in comparison with pure PVDF. The introduction of OA-rGO yielded to membranes with greater porosities rather than when using PFOA-rGO, while PFOA-rGO achieved higher contact angle than its non-fluorinated counterpart OA-rGO. In addition, 0.7% OA-rGO exhibited a stable performance over 162 h of continuous operation, which evidences that this type of membrane is suitable for long-term MD.

Both types of reported MMMs are promising alternatives to replace the commonly used PVDF and PTFE membranes in MD processes, allowing more energy-efficient separation processes (by increasing membrane flux as compared to PVDF) and, as compared to PTFE membranes, MMMs also allow for cutting down the cost and energy consumption during membrane fabrication.

CRediT authorship contribution statement

Jose Miguel Luque-Alled: Conceptualization, Investigation, Methodology, Formal analysis, Data curation, Writing – original draft, Writing – review & editing. **Sebastian Leaper**: Investigation, Methodology, Writing – review & editing. **Ahmed Abdel-Karim**: Investigation, Methodology, Writing – review & editing. **Clara Skuse**: Methodology. **Patricia Gorgojo**: Conceptualization, Supervision, Project administration, Funding acquisition, Writing – review & editing.

Declaration of Competing Interest

The authors declare that they have no known competing financial interests or personal relationships that could have appeared to influence the work reported in this paper.

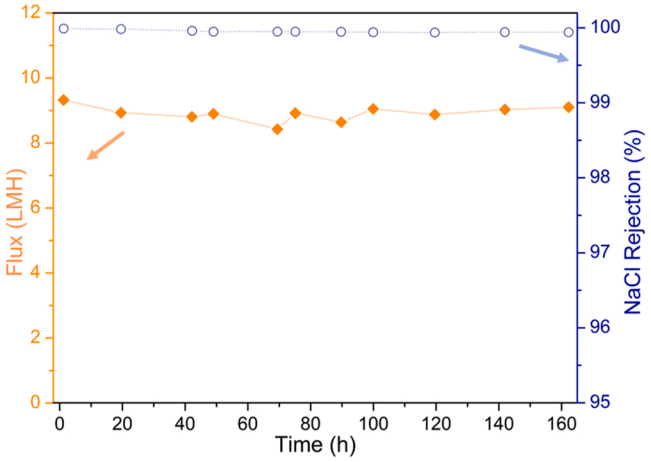

Fig. 10. MD performance of the MMM 0.7% OA-rGO over 162 h of operation. Filled orange diamonds correspond to water flux (L m^{-2} h^{-1}) and unfilled blue circles refer to NaCl rejection (%).

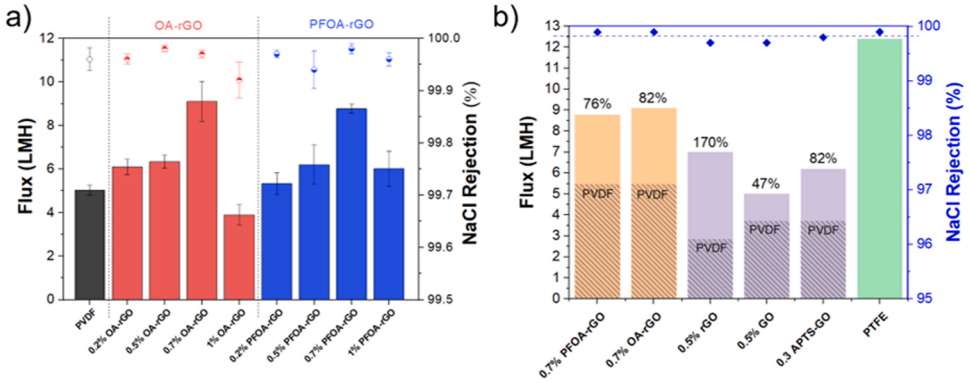

Fig. 9. MD performance of pure PVDF membranes and MMMs containing OA-rGO and PFOA-rGO, where colored bars correspond to flux and symbols to NaCl rejection values (a). Comparison of MD performance of the MMMs in this work that show the highest water flux (0.7% PFOA-rGO and 0.7% OA-rGO), three other PVDF membranes found in the literature containing rGO [13], GO [14] and APTS-GO [14], and commercial PTFE membranes [65]. The solid colored bars represent membrane flux and the diagonal-stripe region corresponds to the flux of the control PVDF membrane used in each particular study. Percentage values above the bars are the calculated flux enhancement in comparison to pure PVDF. The horizontal discontinuous blue line represents a rejection of 99.8%, and blue diamonds refer to rejection values (b).

Data availability

Data will be made available on request.

Acknowledgments

The authors acknowledge the Engineering and Physical Sciences Research Council (EPSRC) grant EP/S032258/1 for supporting this work. Patricia Gorgojo is supported by Grant RYC2019-027060-I funded by MICIN/AEI/10.13039/501100011033 and by "ESF Investing in your future". Jose Miguel Luque-Alled acknowledges the Spanish Ministerio de Economía y Competitividad and the European Social Fund for his Margarita Salas Fellowship, and the Department of Chemical Engineering of the University of Manchester for funding his PhD studies. Authors acknowledge the use of Servicio General de Apoyo a la Investigación-SAI, and the use of instrumentation as well as the technical advice provided by the National Facility ELECMI ICTS, node "Laboratorio de Microscopias Avanzadas (LMA)", both at "Universidad de Zaragoza".

Appendix A. Supporting information

Supplementary data associated with this article can be found in the online version at doi:10.1016/j.jece.2023.109898.

References

[1] V. Ranade, B.V. Industrial, Wastewater treatment, Recycl. Reuse (2014).
[2] V.G. Gude, N. Nirmalakhandan, S.G. Deng, Renewable and sustainable approaches for desalination, Renew. Sustain. Energ. Rev. 14 (9) (2010) 2641–2654, https://doi.org/10.1016/j.rser.2010.06.008.
[3] L.D. Tijing, Y.C. Woo, J.S. Choi, S. Lee, S.H. Kim, H.K. Shon, Fouling and its control in membrane distillation-a review, J. Membr. Sci. 475 (2015) 215–244, https://doi.org/10.1016/j.memsci.2014.09.042.
[4] A. Alkhudhiri, N. Darwish, N. Hilal, Membrane distillation: a comprehensive review, Desalination 287 (2012) 2–18, https://doi.org/10.1016/j.desal.2011.08.027.
[5] Y.D. Kim, K. Thu, S.H. Choi, Solar-assisted multi-stage vacuum membrane distillation system with heat recovery unit, Desalination 367 (2015) 161–171, https://doi.org/10.1016/j.desal.2015.04.003.
[6] R. Miladi, N. Frikha, A. Kheiri, S. Gabsi, Energetic performance analysis of seawater desalination with a solar membrane distillation, Energy Convers. Manag. 185 (2019) 143–154, https://doi.org/10.1016/j.enconman.2019.02.011.
[7] U.K. Kesieme, N. Milne, H. Aral, C.Y. Cheng, M. Duke, Economic analysis of desalination technologies in the context of carbon pricing, and opportunities for membrane distillation, Desalination 323 (2013) 66–74, https://doi.org/10.1016/j.desal.2013.03.033.
[8] S. Al-Obaidani, E. Curcio, F. Macedonio, G. Di Profio, H. Ai-Hinai, E. Drioli, Potential of membrane distillation in seawater desalination: thermal efficiency, sensitivity study and cost estimation, J. Membr. Sci. 323 (1) (2008) 85–98, https://doi.org/10.1016/j.memsci.2008.06.006.
[9] E. Drioli, A. Ali, F. Macedonio, Membrane distillation: recent developments and perspectives, Desalination 356 (2015) 56–84, https://doi.org/10.1016/j.desal.2014.10.028.
[10] P. Wang, T.S. Chung, Recent advances in membrane distillation processes: membrane development, configuration design and application exploring, J. Membr. Sci. 474 (2015) 39–56, https://doi.org/10.1016/j.memsci.2014.09.016.
[11] M. Khayet, Membranes and theoretical modeling of membrane distillation: a review, Adv. Colloid Interface Sci. 164 (1–2) (2011) 56–88, https://doi.org/10.1016/j.cis.2010.09.005.
[12] Z. Cui, E. Drioli, Y.M. Lee, Recent progress in fluoropolymers for membranes, Prog. Polym. Sci. 39 (1) (2014) 164–198, https://doi.org/10.1016/j.progpolymsci.2013.07.008.
[13] A. Abdel-Karim, J.M. Luque-Alled, S. Leaper, M. Alberto, X.L. Fan, A. Vijayaraghavan, T.A. Gad-Allah, A.S. El-Kalliny, G. Szekely, S.I.A. Ahmed, S. M. Holmes, P. Gorgojo, PVDF membranes containing reduced graphene oxide: effect of degree of reduction on membrane distillation performance, Desalination 452 (2019) 196–207, https://doi.org/10.1016/j.desal.2018.11.014.
[14] S. Leaper, A. Abdel-Karim, B. Faki, J.M. Luque-Alled, M. Alberto, A. Vijayaraghavan, S.M. Holmes, G. Szekely, M.I. Badawy, N. Shokri, P. Gorgojo, Flux-enhanced PVDF mixed matrix membranes incorporating APTS-functionalized graphene oxide for membrane distillation, J. Membr. Sci. 554 (2018) 309–323, https://doi.org/10.1016/j.memsci.2018.03.013.
[15] M. Alberto, C. Skuse, M. Tamaddondar, P. Gorgojo, Immobilized graphene oxide-based membranes for improved pore wetting resistance in membrane distillation, Desalination 537 (2022), https://doi.org/10.1016/j.desal.2022.115898.
[16] T.L.S. Silva, S. Morales-Torres, J.L. Figueiredo, A.M.T. Silva, Multi-walled carbon nanotube/PVDF blended membranes with sponge- and finger-like pores for direct contact membrane distillation, Desalination 357 (2015) 233–245, https://doi.org/10.1016/j.desal.2014.11.025.
[17] J. Zahirifar, A. Hadi, J. Karimi-Sabet, A. Dastbaz, Influence of hexagonal boron nitride nanosheets as the additives on the characteristics and performance of PVDF for air gap membrane distillation, Desalination 460 (2019) 81–91, https://doi.org/10.1016/j.desal.2019.03.004.
[18] S. Leaper, E.O.A. Caceres, J.M. Luque-Alled, S.H. Cartmell, P. Gorgojo, POSS-functionalized graphene oxide/PVDF electrospun membranes for complete arsenic removal using membrane distillation, ACS Appl. Polym. Mater. 3 (4) (2021) 1854–1865, https://doi.org/10.1021/acsapm.0c01402.
[19] H.B. Li, W.Y. Shi, X.H. Zeng, S.F. Huang, H.X. Zhang, X.H. Qin, Improved desalination properties of hydrophobic GO-incorporated PVDF electrospun nanofibrous composites for vacuum membrane distillation, Sep. Purif. Technol. 230 (2020) 13, https://doi.org/10.1016/j.seppur.2019.115889.
[20] M. Fouladivanda, J. Karimi-Sabet, F. Abbasi, M.A. Moosavian, Step-by-step improvement of mixed-matrix nanofiber membrane with functionalized graphene oxide for desalination via air-gap membrane distillation, Sep. Purif. Technol. 256 (2021), https://doi.org/10.1016/j.seppur.2020.117809.
[21] L.D. Tijing, J.S. Choi, S. Lee, S.H. Kim, H.K. Shon, Recent progress of membrane distillation using electrospun nanofibrous membrane, J. Membr. Sci. 453 (2014) 435–462, https://doi.org/10.1016/j.memsci.2013.11.022.
[22] L. Zhou, S.H. Tan, A.L. Ahmad, S.C. Low, High-flux strategy for electrospun nanofibers in membrane distillation to treat aquaculture wastewater: a review, J. Chem. Technol. Biotechnol. ⟨https://doi.org/10.1002/jctb.6828⟩.
[23] L.L. Zhong, Y. Wang, D.M. Liu, Z.G. Zhu, W. Wang, Recent advances in membrane distillation using electrospun membranes: advantages, challenges, and outlook, Environ. Sci. Water Res. Technol. 7 (6) (2021) 1002–1019, https://doi.org/10.1039/d1ew00128k.
[24] J.P. Rourke, P.A. Pandey, J.J. Moore, M. Bates, I.A. Kinloch, R.J. Young, N. R. Wilson, The real graphene oxide revealed: stripping the oxidative debris from the graphene-like sheets, Angew. Chem. Int. Ed. Engl. 50 (14) (2011) 3173–3177, https://doi.org/10.1002/anie.201007520.
[25] L.Y. Ng, C.P. Leo, A.W. Mohammad, Optimizing the incorporation of silica nanoparticles in polysulfone/poly(vinyl alcohol) membranes with response surface methodology, J. Appl. Polym. Sci. 121 (3) (2011) 1804–1814, https://doi.org/10.1002/app.33628.
[26] A. Abdel-Karim, T.A. Gad-Allah, A.S. El-Kalliny, S.I.A. Ahmed, E.R. Souaya, M. I. Badawy, M. Ulbricht, Fabrication of modified polyethersulfone membranes for wastewater treatment by submerged membrane bioreactor, Sep. Purif. Technol. 175 (2017) 36–46, https://doi.org/10.1016/j.seppur.2016.10.060.
[27] M. Kumar, Z. Gholamvand, A. Morrissey, K. Nolan, M. Ulbricht, J. Lawler, Preparation and characterization of low fouling novel hybrid ultrafiltration membranes based on the blends of GO - TiO2 nanocomposite and polysulfone for humic acid removal, J. Membr. Sci. 506 (2016) 38–49, https://doi.org/10.1016/j.memsci.2016.02.005.
[28] L.D. Tijing, Y.C. Woo, M.A. Johir, J.S. Choi, H.K. Shon, A novel dual-layer bicomponent electrospun nanofibrous membrane for desalination by direct contact membrane distillation, J. Chem. Eng. 256 (2014) 155–159, https://doi.org/10.1016/j.cej.2014.06.076.
[29] A.E. Khalifa, D.U. Lawal, Application of response surface and Taguchi optimization techniques to air gap membrane distillation for water desalinationA comparative study, Desalin. Water Treat. 57 (59) (2016) 28513–28530, https://doi.org/10.1080/19443994.2016.1189850.
[30] J. Jang, P. Viet Hung, S.H. Hur, J.S. Chung, Dispersibility of reduced alkylamine-functionalized graphene oxides in organic solvents, J. Colloid Interface Sci. 424 (2014) 62–66, https://doi.org/10.1016/j.jcis.2014.03.018.
[31] P. Bandyopadhyay, W.B. Park, R.K. Layek, M.E. Uddin, N.H. Kim, H.-G. Kim, J. H. Lee, Hexylamine functionalized reduced graphene oxide/polyurethane nanocomposite-coated nylon for enhanced hydrogen gas barrier film, J. Membr. Sci. 500 (2016) 106–114, https://doi.org/10.1016/j.memsci.2015.11.029.
[32] X. Yang, T. Mei, J. Yang, C. Zhang, M. Lv, X. Wang, Synthesis and characterization of alkylamine-functionalized graphene for polyolefin-based nanocomposites, Appl. Surf. Sci. 305 (2014) 725–731, https://doi.org/10.1016/j.apsusc.2014.03.184.
[33] Y. Zhang, B. Yang, K.L. Li, D.Y. Hou, C.W. Zhao, J. Wang, Electrospun porous poly (tetrafluoroethylene-co-hexafluoropropylene-co-vinylidene fluoride) membranes for membrane distillation, RSC Adv. 7 (89) (2017) 56183–56193, https://doi.org/10.1039/c7ra09932k.
[34] C.P. Ennis, R.I. Kaiser, Mechanistical studies on the electron-induced degradation of polymers: polyethylene, polytetrafluoroethylene, and polystyrene, Phys. Chem. Chem. Phys. 12 (45) (2010) 14884–14901, https://doi.org/10.1039/c0cp00493f.
[35] H. Wang, Y.F. Wen, H.Y. Peng, C.F. Zheng, Y.S. Li, S. Wang, S.F. Sun, X.L. Xie, X. P. Zhou, Grafting polytetrafluoroethylene micropowder via in situ electron beam irradiation-induced polymerization, Polymers 10 (5) (2018), https://doi.org/10.3390/polym10050503.
[36] M. Wen, M. Chen, G.K. Ren, P.L. Li, C. Lv, Y. Yao, Y.K. Liu, S.J. Deng, Z. Zheng, C. G. Xu, D.L. Luo, Enhancing the selectivity of hydrogen isotopic water in membrane distillation by using graphene oxide, J. Membr. Sci. 610 (2020) 11, https://doi.org/10.1016/j.memsci.2020.118237.
[37] M. Alberto, J.M. Luque-Alled, L. Gao, M. Iliut, E. Prestat, L. Newman, S.J. Haigh, A. Vijayaraghavan, P.M. Budd, P. Gorgojo, Enhanced organophilic separations with mixed matrix membranes of polymers of intrinsic microporosity and graphene-like fillers, J. Membr. Sci. 526 (2017) 437–449, https://doi.org/10.1016/j.memsci.2016.12.061.
[38] T.J. Bao, Z.Y. Wang, Y. Zhao, Y. Wang, X.S. Yi, Composition, structure and morphology evolution of octadecylamine (ODA)-reduced graphene oxide and its

dispersion stability under different reaction conditions, Materials 11 (9) (2018), https://doi.org/10.3390/ma11091710.
[39] G. Chen, J.Y. Zhang, S.R. Yang, Fabrication of hydrophobic fluorinated amorphous carbon thin films by an electrochemical route, Electrochem. Commun. 10 (1) (2008) 7–11, https://doi.org/10.1016/j.elecom.2007.10.006.
[40] F.G. Zhao, G. Zhao, X.H. Liu, C.W. Ge, J.T. Wang, B.L. Li, Q.G. Wang, W.S. Li, Q. Y. Chen, Fluorinated graphene: facile solution preparation and tailorable properties by fluorine-content tuning, J. Mater. Chem. A 2 (23) (2014) 8782–8789, https://doi.org/10.1039/c4ta00847b.
[41] A.M. Ferraria, J.D.L. da Silva, A.M.B. do Rego, XPS studies of directly fluorinated HDPE: problems and solutions, Polymer 44 (23) (2003) 7241–7249, https://doi.org/10.1016/j.polymer.2003.08.038.
[42] O.C. Compton, D.A. Dikin, K.W. Putz, L.C. Brinson, S.T. Nguyen, Electrically conductive "alkylated" graphene paper via chemical reduction of amine-functionalized graphene oxide paper, Adv. Mater. 22 (8) (2010) 892, https://doi.org/10.1002/adma.200902069.
[43] J. Huang, S.M. Ding, W.M. Xiao, Y.D. Peng, S.J. Deng, N. Zhang, 3-Aminopropyl-triethoxysilane functionalized graphene oxide: a highly efficient and recyclable catalyst for knoevenagel condensation, Catal. Lett. 145 (4) (2015) 1000–1007, https://doi.org/10.1007/s10562-014-1461-8.
[44] J.M. Luque-Alled, A. Ameen, M. Alberto, M. Tamaddondar, A.B. Foster, P.M. Budd, A. Vijayaraghavan, P. Gorgojo, Gas separation performance of MMMs containing (PIM-1)-functionalized GO derivatives, J. Membr. Sci. (2020).
[45] L.G. Guex, B. Sacchi, K.F. Peuvot, R.L. Andersson, A.M. Pourrahimi, V. Strom, S. Farris, R.T. Olsson, Experimental review: chemical reduction of graphene oxide (GO) to reduced graphene oxide (rGO) by aqueous chemistry, Nanoscale 9 (27) (2017) 9562–9571, https://doi.org/10.1039/c7nr02943h.
[46] H. He, Y.J. Hu, S.X. Chen, L.Z. Zhuang, B.B. Ma, Q.H. Wu, Preparation and properties of a hyperbranch-structured polyamine adsorbent for carbon dioxide capture, Sci. Rep. 7 (2017), https://doi.org/10.1038/s41598-017-04329-w.
[47] F.L. Zhou, H.N. Tien, Q.B. Dong, W.W.L. Xu, H.Z. Li, S.G. Li, M. Yu, Ultrathin, ethylenediamine-functionalized graphene oxide membranes on hollow fibers for CO_2 capture, J. Membr. Sci. 573 (2019) 184–191, https://doi.org/10.1016/j.memsci.2018.11.080.
[48] S. Mohsenpour, S. Leaper, J. Shokri, M. Alberto, P. Gorgojo, Effect of graphene oxide in the formation of polymeric asymmetric membranes via phase inversion, J. Membr. Sci. 641 (2022), https://doi.org/10.1016/j.memsci.2021.119924.
[49] M. Romay, N. Diban, M.J. Rivero, A. Urtiaga, I. Ortiz, Critical issues and guidelines to improve the performance of photocatalytic polymeric membranes, Catalysts 10 (5) (2020), https://doi.org/10.3390/catal10050570.
[50] Y.Chuanqi Zhao, Xiaochen Xu, Jie Chen, Fenglin, Effect of graphene oxide concentration on the morphologies and antifouling properties of PVDF ultrafiltration membranes, J. Environ. Chem. Eng. 1 (2013) 349–354, https://doi.org/10.1016/j.jece.2013.05.014.
[51] V.H. Dalvi, P.J. Rossky, Molecular origins of fluorocarbon hydrophobicity, Proc. Natl. Acad. Sci. USA 107 (31) (2010) 13603–13607, https://doi.org/10.1073/pnas.0915169107.
[52] J.C. Biffinger, H.W. Kim, S.G. DiMagno, The polar hydrophobicity of fluorinated compounds, Chembiochem 5 (5) (2004) 622–627, https://doi.org/10.1002/cbic.200300910.
[53] C.Y. Ng, L.H. Khoo, L.Y. Ng, C.B. Ong, E. Mahmoudi, R. Rohani, A.W. Mohammad, Novel polyethersulfone-cellulose composite thin film using sustainable empty fruit bunches from Elaeis guineensis for methylene blue removal, Polym. Test. 86 (2020), https://doi.org/10.1016/j.polymertesting.2020.106494.
[54] X.M. Cai, T.P. Lei, D.H. Sun, L.W. Lin, A critical analysis of the alpha, beta and gamma phases in poly(vinylidene fluoride) using FTIR, RSC Adv. 7 (25) (2017) 15382–15389, https://doi.org/10.1039/c7ra01267e.
[55] B.Ja.A. Jabbari, Evaluation of reduced graphene oxide/ZnO effect on properties of PVDF nanocomposite films, Appl. Surf. Sci. 320 (2014) 339–347, https://doi.org/10.1016/j.apsusc.2014.09.030.
[56] A.A. Issa, M.A.S. Al-Maadeed, M. Mrlik, A.S. Luyt, Electrospun PVDF graphene oxide composite fibre mats with tunable physical properties, J. Polym. Res. 23 (8) (2016), https://doi.org/10.1007/s10965-016-1126-y.
[57] S.X. Song, Z.H. Zheng, Y.J. Bi, X. Lv, S.L. Sun, Improving the electroactive phase, thermal and dielectric properties of PVDF/graphene oxide composites by using methyl methacrylate-co-glycidyl methacrylate copolymers as compatibilizer, J. Mater. Sci. 54 (5) (2019) 3832–3846, https://doi.org/10.1007/s10853-018-3075-9.
[58] K. Sabira, P. Saheeda, M.C. Divyasree, S. Jayalekshmi, Impressive nonlinear optical response exhibited by Poly(vinylidene fluoride) (PVDF)/reduced graphene oxide (RGO) nanocomposite films, Opt. Laser Technol. 97 (2017) 77–83, https://doi.org/10.1016/j.optlastec.2017.06.008.
[59] S. Alyarnezhad, T. Marino, J.B. Parsa, F. Galiano, C. Ursino, H. Garcia, M. Puche, A. Figoli, Polyvinylidene fluoride-graphene oxide membranes for dye removal under visible light irradiation, Polymers 12 (7) (2020), https://doi.org/10.3390/polym12071509.
[60] M. Baghbanzadeh, D. Rana, C.Q. Lan, T. Matsuura, Effects of hydrophilic silica nanoparticles and backing material in improving the structure and performance of VMD PVDF membranes, Sep. Purif. Technol. 157 (2016) 60–71, https://doi.org/10.1016/j.seppur.2015.11.029.
[61] R.F. Zhou, D. Rana, T. Matsuura, C.Q. Lan, Effects of multi-walled carbon nanotubes (MWCNTs) and integrated MWCNTs/SiO2 nano-additives on PVDF polymeric membranes for vacuum membrane distillation, Sep. Purif. Technol. 217 (2019) 154–163, https://doi.org/10.1016/j.seppur.2019.02.013.
[62] J.E. Efome, D. Rana, T. Matsuura, C.Q. Lan, Enhanced performance of PVDF nanocomposite membrane by nanofiber coating: a membrane for sustainable desalination through MD, Water Res. 89 (2016) 39–49, https://doi.org/10.1016/j.watres.2015.11.040.
[63] L. Eykens, K. De Sitter, C. Dotremont, L. Pinoy, B. Van der Bruggen, How to optimize the membrane properties for membrane distillation: a review, Ind. Eng. Chem. Res. 55 (35) (2016) 9333–9343, https://doi.org/10.1021/acs.iecr.6b02226.
[64] K.J. Lu, J. Zuo, T.S. Chung, Novel PVDF membranes comprising n-butylamine functionalized graphene oxide for direct contact membrane distillation, J. Membr. Sci. 539 (2017) 34–42, https://doi.org/10.1016/j.memsci.2017.05.064.
[65] S. Leaper, A. Abdel-Karim, T.A. Gad-Allah, P. Gorgojo, Air-gap membrane distillation as a one-step process for textile wastewater treatment, J. Chem. Eng. 360 (2019) 1330–1340, https://doi.org/10.1016/j.cej.2018.10.209.
[66] Y.C. Woo, Y. Kim, W.G. Shim, L.D. Tijing, M.W. Yao, L.D. Nghiem, J.S. Choi, S. H. Kim, H.K. Shon, Graphene/PVDF flat-sheet membrane for the treatment of RO brine from coal seam gas produced water by air gap membrane distillation, J. Membr. Sci. 513 (2016) 74–84, https://doi.org/10.1016/j.memsci.2016.04.014.
[67] J.M. Luque-Alled, A. Abdel-Karim, M. Alberto, S. Leaper, M. Perez-Page, K. Huang, A. Vijayaraghavan, A.S. El-Kalliny, S.M. Holmes, P. Gorgoj, Polyethersulfone membranes: from ultrafiltration to nanofiltration via the incorporation of APTS functionalized-graphene oxide, Sep. Purif. Technol. 230 (2020), https://doi.org/10.1016/j.seppur.2019.115836.
[68] F.A. AlMarzooqi, M.R. Bilad, H. Arafat, Improving liquid entry pressure of polyvinylidene fluoride (PVDF) membranes by exploiting the role of fabrication parameters in vapor-induced phase separation VIPS and non-solvent-induced phase separation (NIPS) processes, Appl. Sci. 7 (2) (2017), https://doi.org/10.3390/app7020181.